CrossMark

Morphology-controllable synthesis, energy transfer and luminescence properties of Ce^{3+}/Tb^{3+}/Eu^{3+}-doped CaF$_2$ microcrystals

Bei Zhao[1], Dingyi Shen[1], Qinyue Tan[1], Jianfeng Tang[2], Xianju Zhou[3], Shanshan Hu[1,*], and Jun Yang[1,*]

[1] School of Chemistry and Chemical Engineering, Southwest University, No. 2 Tiansheng Road, Beibei District, Chongqing 400715, People's Republic of China
[2] Faculty of Materials and Energy, Southwest University, Chongqing 400715, People's Republic of China
[3] School of Mathematics and Physics, Chongqing University of Posts and Telecommunications, Chongqing 400065, People's Republic of China

ABSTRACT

CaF$_2$:Ln^{3+} (Ln = Ce, Tb, Eu) phosphors with highly uniform shapes have been successfully synthesized by a simple hydrothermal method directly. The as-prepared samples were characterized by X-ray diffraction (XRD), scanning electron microscopy (SEM), photoluminescence (PL) and lifetime. The results indicated that the pH values, organic additive and reaction time have a significant effect on the morphology and dimensions of CaF$_2$ microcrystals and the possible formation mechanism was also proposed. Furthermore, the energy transfer from Ce^{3+} to Tb^{3+} and from Tb^{3+} to Eu^{3+} and from Ce^{3+} to Tb^{3+} to Eu^{3+} was observed and the corresponding mechanisms were discussed in detail. The CaF$_2$:Ln^{3+} phosphors may have potential optical applications in near-UV and violet LEDs.

Introduction

In general, the chemical composition, size, phase, surface chemistry, shape and dimensionality of inorganic micro-/nanostructure of phosphors have great influence on their chemical and physical properties [1]. Therefore, more and more chemists pay attention to the reasonable control of these factors, which allowed us not only to own peculiar properties of the materials, but also to modify their chemical and physical properties as needed [2]. The phosphors with perfect luminescent performance require the dimensions of phosphors that should be in the range 1–3 μm with ideal spherical particles [3, 4] because of their unique properties (e.g., high packing densities, high surface-to-volume ratio and low scattering of light) and widespread applications in white light-emitting diodes (WLEDs), field emission displays (FEDs) and cathode ray tubes (CRTs) [5–7]. So far, the spherical phosphors can be obtained by many synthetic methods including spray pyrolysis, sol–gel

Address correspondence to E-mail: hushan3@swu.edu.cn; jyang@swu.edu.cn

🖄 Springer

process, urea homogeneous precipitation [8, 9]. However, these methods have many disadvantages such as low yield, large crystallites long reaction time and high environment loads [5, 10]. Compared with the methods mentioned above, the hydrothermal method provides a relatively green chemical alternative to preparation of various nano-/micromaterials. Meanwhile, the method has a number of other merits such as simplicity, safety, convenience and controllable size/phase/morphology of the products [11].

Inorganic fluoride materials have attracted a great deal of interest for their potential applications in labels, optics, components of gate dielectrics and insulators [12, 13] owing to their merits such as high resistivity, low-energy phonons, electron-acceptor behavior, high iconicity and anionic conductivity, compared with other oxide or sulfide materials [14–17]. Among the various fluorides, calcium fluoride (CaF_2) has attracted more and more attention because of its wide band gap (Eg = 12.1 eV), low refractive index and optically transparent over a wide wavelength range from mid-infrared to vacuum ultraviolet [18, 19]. So, it is widely used in UV-transparent optical lenses, UV lithography, biocompatible luminescent markers and surface conditioning of glass [13, 19, 20]. Moreover, CaF_2 is an attractive host for phosphors activated with rare-earth ions (RE^{3+}), which display unique up-/down-conversion luminescence properties arising from their 4f electron configuration [21]. Various CaF_2 with different structures including films, nanocrystals, nanowires, nanocubes, nanoparticles and 3D flower-like nanostructures have been successfully fabricated by multiple methods [12, 14, 21–25].

In present, the shortage of line-emitting red phosphors (above 600 nm) [26] which can improve rendering index in white light package [27] in LEDs is still a big problem. Owing to Eu^{3+}-activated phosphors with excellent red color purity of $^5D_0 \rightarrow \, ^7F_J$ transitions, they are supposed to red-emitting phosphors with high efficiency. However, the low oscillator strength and narrow line width of Eu^{3+} $4f \rightarrow 4f$ absorption transitions lead to a weak absorption in the near-UV and blue region [28]. Thus, it is necessary to find sensitizers with strong and broad excitation bands in the typical emission wavelength of GaN-based LEDs (350–450 nm) for Eu^{3+} luminescence. Taking into account of metal–metal charge transfer (MMCT) quenching [29], direct sensitization of Eu^{3+}

luminescence with Ce^{3+} is unlikely. As mentioned in the previous literature [30], the $Ce^{3+} \rightarrow Tb^{3+} \rightarrow Eu^{3+}$ energy-transfer (ET) scheme can produce Eu^{3+} red phosphors, which are regarded as potential candidates for down-converting phosphors in the field of near-UV and violet LEDs because of their strong absorption bands in the near-UV and violet spectral regions. The luminescent properties of $Er^{3+}/Tm^{3+}/Yb^{3+}$-doped CaF_2 [25], Ce^{3+}/Tb^{3+}-codoped CaF_2 [31, 32] and Tb^{3+}/Eu^{3+}-codoped CaF_2 [33] have also been studied. Energy transfer between the doped luminescent ions in the solid materials has great influence on enhancing luminescent emission and excitation efficiency [34]. To the best of our knowledge, the energy transfer of $Ce^{3+} \rightarrow Tb^{3+} \rightarrow Eu^{3+}$ in CaF_2 materials by hydrothermal method has little been reported in the previous literature [12, 14, 21–25, 31–34].

Herein, it is very useful for practical applications that self-assembled $CaF_2:Ce^{3+}/Tb^{3+}/Eu^{3+}$ microspheres composed of nanoparticles not only possess the desirable properties of nanocrystals but also have the quite stable form of microspheres and solve the problem of nanomaterial agglomeration. Various morphologies of CaF_2 phosphors can be achieved by simple tuning several critical parameters including pH, organic additive and reaction time. Meanwhile, the growth mechanism for the microspheres has been proposed. Moreover, we also investigate the energy-transfer process of $Ce^{3+} \rightarrow Tb^{3+}$, $Tb^{3+} \rightarrow Eu^{3+}$ and $Ce^{3+} \rightarrow Tb^{3+} \rightarrow Eu^{3+}$ in CaF_2 phosphors in detail. The transfer efficiency is 90.5% ($Ce^{3+} \rightarrow Tb^{3+}$) and 89.5% ($Ce^{3+} \rightarrow Tb^{3+} \rightarrow Eu^{3+}$), respectively. In addition, the ET process is systematically discussed based on the decay times of Ce^{3+} and Tb^{3+}. The results indicate that the energy transfer of $Ce^{3+} \rightarrow Tb^{3+} \rightarrow Eu^{3+}$ in CaF_2 successfully makes it as potential down-converting phosphor candidates for near-UV and violet LEDs [35].

Experimental section

Preparation

All chemicals were purchased from Aladdin and used directly without further purification. The Eu_2O_3 (99.99%), Tb_4O_7 (99.99%), CeO_2 (99.99%) were dissolved in hot diluted HNO_3 solution under constant stirring followed by evaporation of excessive HNO_3 to form $Ln(NO_3)_3$ (Ln = Ce, Tb, Eu) solutions (0.1 mol/L); however, in the process of dissolving

CeO$_2$ in hot diluted HNO$_3$ solution, the H$_2$O$_2$ solution was continuously added to the above solution. A typical procedure was described as follows: Firstly, 2 mmol of Ca(NO$_3$)$_2$·4H$_2$O was added to 25 mL distilled water at room temperature, followed by the addition of 4 mmol of sodium citrate to form an optically transparent solution. Then, 15 mL of aqueous solution containing 4 mmol of NaBF$_4$ was added to the mixture under vigorous stirring. After that, HNO$_3$ was dropwise introduced to the vigorous stirred solution to keep pH = 6.5. Sequentially, the mixture was agitated for another 30 min and transferred into a 50-mL autoclave, heated at 180 °C for 24 h and cooled naturally to room temperature. Finally, the precipitates were washed, centrifuged for several times with distilled water and absolute ethanol in turn, then dried at 60 °C for 8 h and crushed in an agate mortar to obtain samples which was denoted as S_1. Additionally, rare-earth nitrate solutions of 0.1 mol/L (Ce, Tb, Eu) were added into the solution to form CaF$_2$:Ln^{3+} (Ln = Ce, Tb, Eu). The typical synthetic samples with experimental parameters are listed in Table S1 (Supporting Information).

Characterizations

All measurements were taken at room temperature. X-ray power diffraction (XRD) measurements were taken on a Purkinje General Instrument MSALXD3 using Cu Kα radiation ($\lambda = 0.15406$ nm). The morphology analysis was carried out on a field emission scanning electron microscopy (FESEM, Hitachi, S-4800). The PL excitation and emission spectra were detected by an F-7000 spectrophotometer (Hitachi, Japan) equipped with a 150-W xenon lamp as excitation source. The luminescence decays were measured on a FLSP920 fluorescence spectrophotometer.

Results and discussion

Phase and morphology

Effects of pH values

The composition and phase purity of the products which were prepared using Cit^{3-} as organic additive and synthesized with hydrothermal treatment at 180 °C for 24 h under various pH conditions were first investigated by XRD. The XRD patterns of the

samples and the standard data of CaF$_2$ (JCPDS No. 35-0816) are shown in Fig. 1. We can see that all the diffraction peaks of the obtained products coincide well with the standard data of CaF$_2$ (JCPDS 35-0816), which can be attributable to pure cubic phase. The sharp diffraction peaks indicate that these four samples are well crystallized at a relatively low hydrothermal treatment temperature (180 °C). It can be seen that the XRD peaks of the four samples show slight shift with respect to those of CaF$_2$ in the JCPDS card. This may be caused by the minor alteration of the cell parameters of CaF$_2$ crystals grown under different conditions or the instrument errors.

The representative low-magnification SEM images of CaF$_2$ prepared by using Cit^{3-} as organic additive at different pH values are exhibited in Fig. 2. The size of CaF$_2$ microcrystals is critically dependent on the pH value during the hydrothermal process. It is clear that all the CaF$_2$ microcrystals prepared at different pH values are spherical in shape. At pH = 5, the uneven CaF$_2$ microspheres (S_2) with size of 410 nm–1.7 μm in diameter are observed from Fig. 2a. When the pH value of the initial solution is 8, the general image of CaF$_2$ microspheres (S_3) is shown in Fig. 2c. The diameter of the particles is from 330 nm to 1.4 μm. Upon a further increase of the pH value up to 9, the CaF$_2$ microspheres (S_4) have a mean diameter from 380 nm to 1.9 μm (Fig. 2d). When the experiment is performed at pH = 6.5 adjusted with HNO$_3$ solution and other experimental conditions remain unchanged, it clearly indicates that the products (S_1)
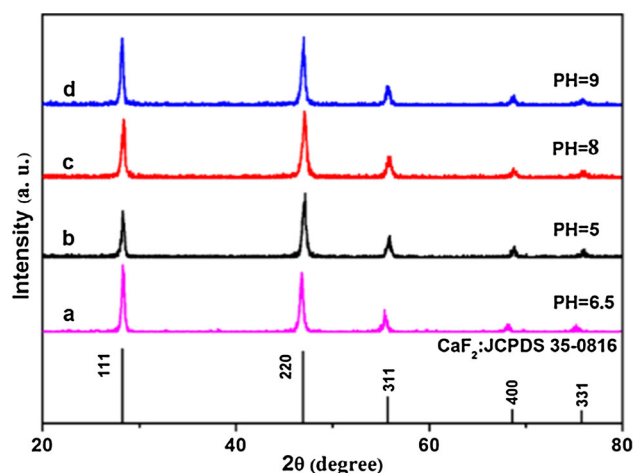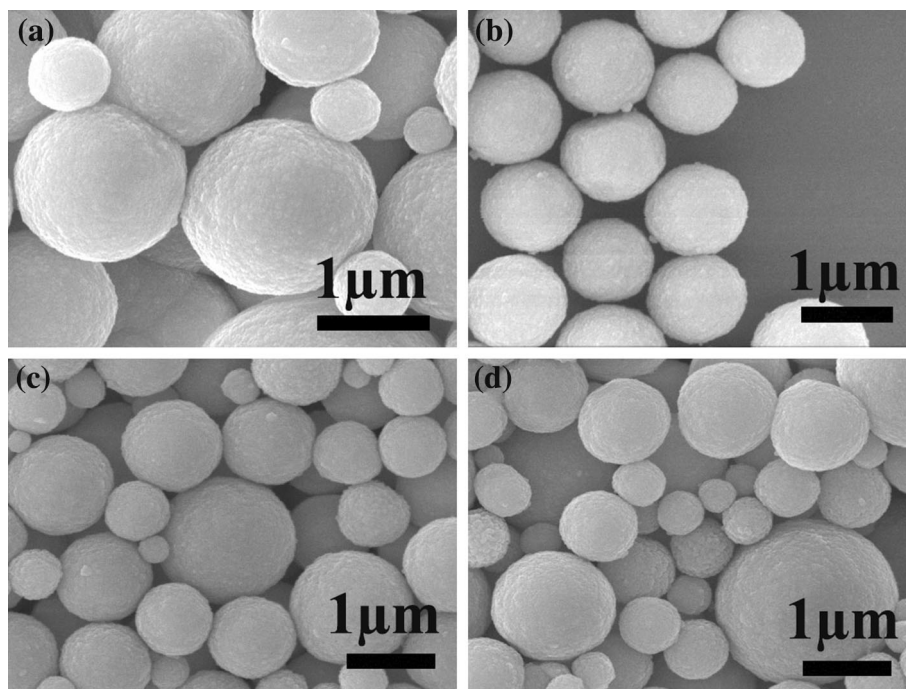

Figure 1 The XRD patterns of the as-prepared CaF$_2$ products using Cit^{3-} as an organic additive for 24 h at 180 °C with different pH values of *a* 6.5, *b* 5 and *c* 8, *d* 9.

Figure 2 SEM images of CaF$_2$ samples obtained with Cit^{3-} as an organic additive at different pH values **a** 5, **b** 6.5, **c** 8 and **d** 9.

are composed of remarkable uniformity and monodisperse microspheres (Fig. 2b) with uniform size of 1 μm in diameter. The surface of microspheres is not smooth and contains many dense nanoparticles. From the above analysis, it can be concluded that the size of microspheres decreases generally with the increase of pH value. The reason for that can be ascribed to the different interactions of Cit^{3-} with CaF$_2$-specific crystal planes under different pH [36] which leads to different crystal growth rates during the complicated hydrothermal process [37]. It was reported that the pH value of the precursor solution could effectively affect the balance between the chemical potential and the rate of ionic migration in the precursor solution, and affect the morphology and size of the products [38]. For CaF$_2$ microspheres, a low pH value results in a fast crystal growth and leads to a large crystal size (Fig. 2a). On the contrary, a high pH value is beneficial to a fast nucleation and thus the generation of a large number of crystal nuclei, resulting in crystals with a small size (Fig. 2d).

Effects of additives

As shown in Fig. 3, the samples of CaF$_2$ prepared under various organic additive conditions were first examined by XRD. All the diffraction peaks correspond to the JCPDS No. 35-0816 of pure cubic phase
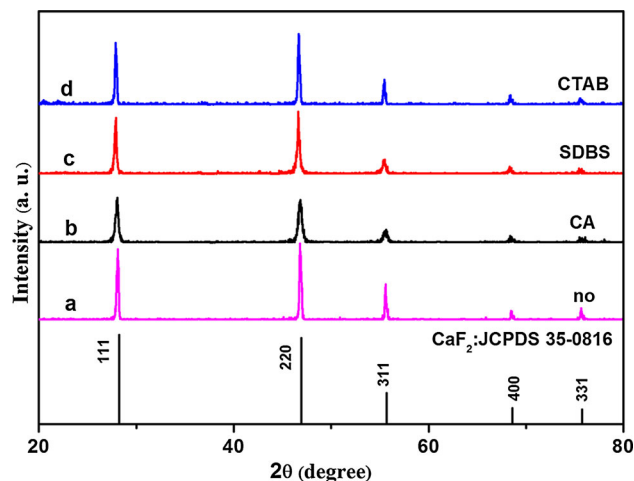

Figure 3 XRD patterns of CaF$_2$ products prepared under the identical conditions except using different organic additive: CA (*b*), SDBS (*c*), CTAB (*d*) and the absence of organic additive (*a*).

of CaF$_2$. The strong and sharp diffraction peaks of the samples indicate that as-prepared nanocrystals are well crystallized. However, the diffraction peaks of products without organic additive (Fig. 3a) are much sharper than those of products using organic additive (Figs. 3b–d and 1a). The similarity of XRD patterns indicates the negligible influence of the used organic additive on phase of cubic CaF$_2$.

The direct impact of organic additive on morphologies of CaF$_2$ can be observed in their SEM

Figure 4 SEM images of CaF$_2$ samples obtained at pH = 6.5 (180 °C, 24 h) using different organic additives, **a**, **b** without additive, **c**, **d** CA, **e**, **f** SDBS and **g**, **h** CTAB.
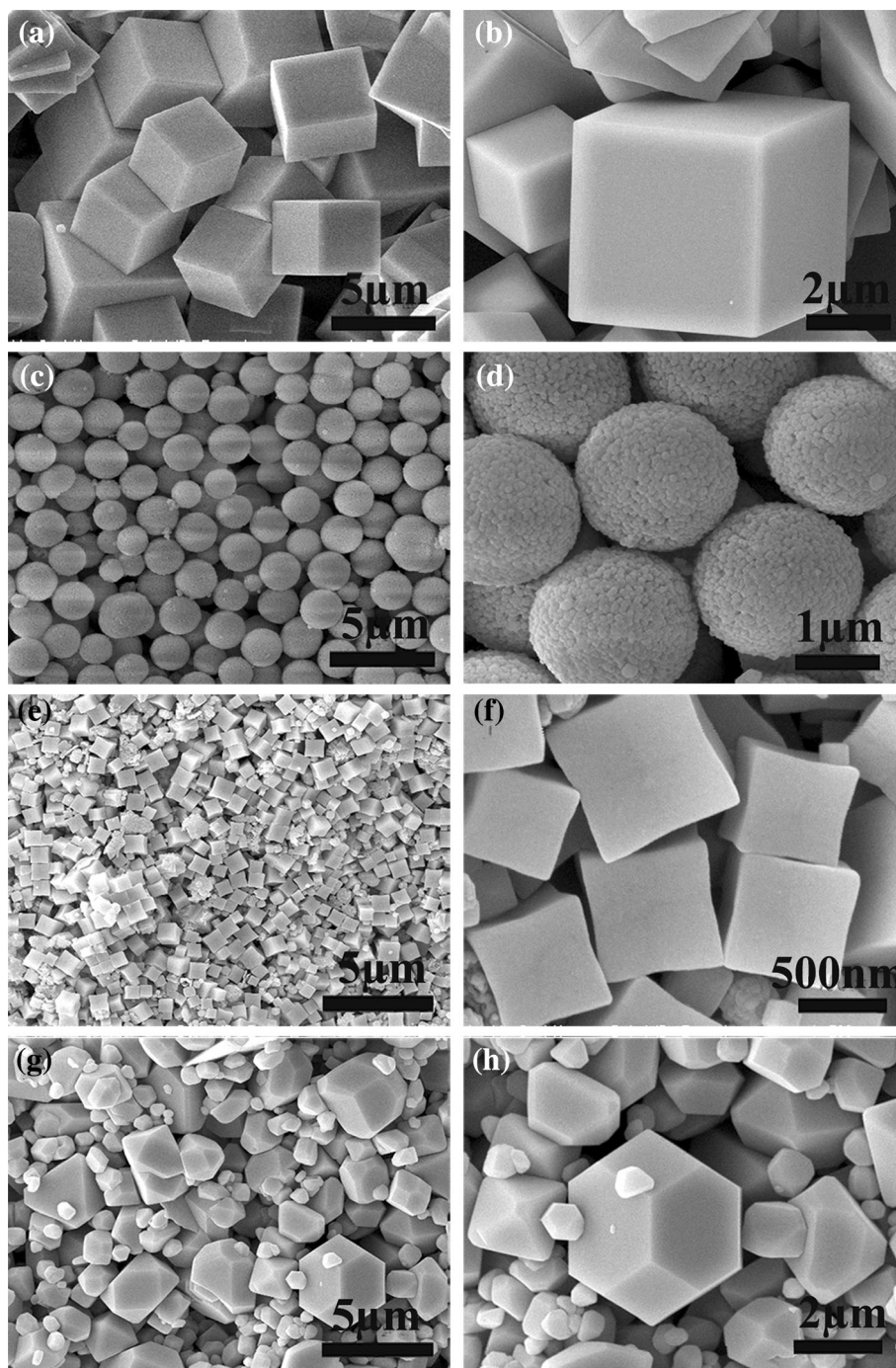
images (Fig. 4). In the absence of organic additive, it is found that the morphology of the as-prepared CaF$_2$ consists of highly dispersed cubes with edge length of 3 μm (Fig. 4a, b). When 0.8416 g CA is added, uniform spheres with average size of 2 μm in diameter are observed from Fig. 4c. The high-magnification SEM image (Fig. 4d) of the CaF$_2$ microspheres provides detailed structural information on the

spheres. The peripheral surface of individual spheres is not smooth and contains many dense nanoparticles. In order to investigate the effect of organic additives further, other organic additives, SDBS and CTAB, are used to synthesize CaF$_2$ by an identical procedure. When SDBS is used as organic additive, the CaF$_2$ cube with the concave in the middle of the surface is formed (Fig. 4e) and its size is 700 nm

(Fig. 4f). While the other experimental conditions are identical and CTAB acts as organic additive, the crystal shapes of the samples are quite different. As shown in Fig. 4g, h the sample is of a similar shape. The truncated irregular octahedron can be observed, and a large number of heterogeneous dispersed polyhedron with the edge length about 400 nm–3.8 μm are formed. These results indicate that the morphologies of the CaF_2 microstructures are sensitive to organic additives. The reasons may be as follows: On the one hand, the differences of the chelating constants of various organic additives with Ca^{2+} lead to the different nucleation rates of CaF_2; on the other hand, various organic additives selectively adsorb on the specific crystal facets of CaF_2 particles which result in the different growth rates of different facets, and then form the different morphologies and sizes.

Effects of reaction time

For the better understanding of the growth mechanism of CaF_2 microspheres, time-dependent experiments were carried out (pH = 6.5) by using Cit^{3-} as organic additive at 180 °C for 2, 4, 8 and 24 h, respectively (Fig. 5). The SEM images clearly show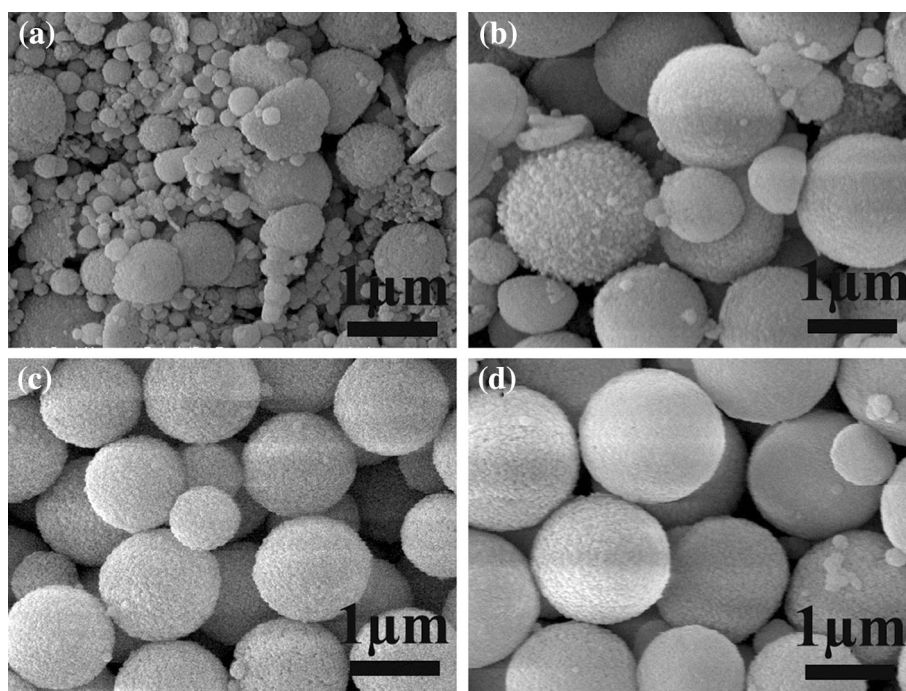 a typical process of the microspherical structure which is obtained by the self-assembly of the primary nanoparticles to form the final products. After hydrothermal treatment of 2 h, the sample obtained is primary particle which consists of random nanoparticles (Fig. 5a). At a reaction time of 4 h, the products consist of spherical-like particles with a mean diameter of 800 nm (Fig. 5b). It proves that the particle aggregates by the growth of crystal nucleus on different direction (random aggregation) to form spherical crystals. Figure 4c is the image of the sample with reaction time of 8 h; microspheres with an average size of 1.2 μm are formed and become bigger due to isotropic growth at the expense of nanoparticles. Finally, after hydrothermal treatment of 24 h (Fig. 5d), the spherical crystals have become more uniform after further growth and recrystallization.
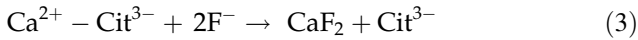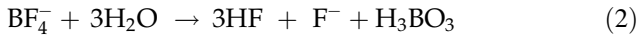
The possible formation mechanism for the CaF_2 microspheres

Based on the above experimental results, the probable reaction process for the formation of CaF_2 microspheres using Cit^{3-} as organic additive at pH = 6.5 may be summarized as Eqs. (1)–(3):

$$Ca^{2+} + Cit^{3-} \rightarrow Ca^{2+} - Cit^{3-} \tag{1}$$

Figure 5 SEM images of the as-prepared CaF_2 samples with Cit^{3-} as organic additive at 180 °C for different reaction times: **a** 2 h, **b** 4 h, **c** 8 h and **d** 24 h.

$$BF_4^- + 3H_2O \rightarrow 3HF + F^- + H_3BO_3 \qquad (2)$$

$$Ca^{2+} - Cit^{3-} + 2F^- \rightarrow CaF_2 + Cit^{3-} \qquad (3)$$

As is well known, the formation of a particle includes the initial production, subsequent growth and final stabilization of nuclei; the morphology and size of particles are mainly determined by the nucleation rate [33]. The detailed formation process of the CaF_2 microspheres can be summarized as follows: In the early stage of the reaction, Ca^{2+} and Cit^{3-} formed Ca^{2+}–Cit^{3-} as the intermediate which not only affect the morphology of the product but also afford a reactant source for an interfacial reaction. With the addition of $NaBF_4$, Ca^{2+} could be released into the solution because the bond Ca^{2+}–Cit^{3-} could be destroyed by anions BO_3^{3-} and BF_4^-; then the F^- ions deposited onto the surface of the intermediate and reacted with the Ca^{2+} to generate CaF_2 nuclei under hydrothermal treatment. As a result, the CaF_2 nuclei were formed by surface deposition and a subsequent crystal growth process; further, the nonuniform particles were obtained due to particles growing quickly after nucleation. As the reaction continued, the CaF_2 nuclei aggregated each other to form CaF_2 particles with the consumption of intermediate gradually. Finally, the CaF_2 particle size was uniform and the adjacent particles could connect with each other to form the CaF_2 microspheres with enough ripening time due to the higher surface energy. The formation mechanism of the CaF_2 spheres depends on a series of chemical and structural transformations. During the process, Cit^{3-} plays a key role in controlling the morphology of the final CaF_2 products.

Luminescence properties and energy transfer

The self-assembled CaF_2 microspheres are beneficial to obtain the ideal luminescent properties, because the narrow size distribution and good dispersivity of spherical CaF_2: Ln^{3+} phosphors lead to high brightness, high resolution, low scattering and high packing densities of light [33].

Figure 6 demonstrates the photoluminescence excitation (PLE) and emission (PL) spectra of Ce^{3+} and Tb^{3+} single-doped and Ce^{3+}/Tb^{3+} co-doped CaF_2 phosphors. As shown in Fig. 6a, when monitored at 359 nm, the CaF_2:2%Ce^{3+} sample exhibits a broad and strong band with a maximum at 304 nm and a weaker band at 251 nm which are assigned to the electron transition from the 4f energy level to different 5d sublevels of the Ce^{3+}. The PL spectrum has an asymmetric blue broadband ranging from 320 to 600 nm with a peak at 359 nm which is assigned to the f–d absorption of the Ce^{3+} ions. The broad and asymmetric emission bands of CaF_2:2%Ce^{3+} can be attributed to the transitions of the Ce^{3+} ions occupying two Ca^{2+} ion sites in the host structure. As shown in Fig. 6b, the PLE spectrum monitored at 544 nm for CaF_2:4%Tb^{3+} sample presents a strong band at 215 nm and a weak band at 259 nm which correspond to the spin-allowed ($\Delta S = 0$) and spin-forbidden ($\Delta S = 1$) components of the $4f^8$–$4f^75d$ transition [39], respectively. On excitation into the $4f^8$–$4f^75d$ transition at 215 nm, the PL spectrum consists of emission lines at 494 nm ($^5D_4 \rightarrow {}^7F_6$) in the blue region and 544 nm ($^5D_4 \rightarrow {}^7F_5$) in the green region, as well as 590 nm ($^5D_4 \rightarrow {}^7F_4$) and 626 nm ($^5D_4 \rightarrow {}^7F_3$) in the red region. The intensity of

Figure 6 PLE and PL spectra of CaF_2: 2%Ce^{3+} (*a*), 4%Tb^{3+} (*b*) and 2%Ce^{3+}/4%Tb^{3+} (*c*).
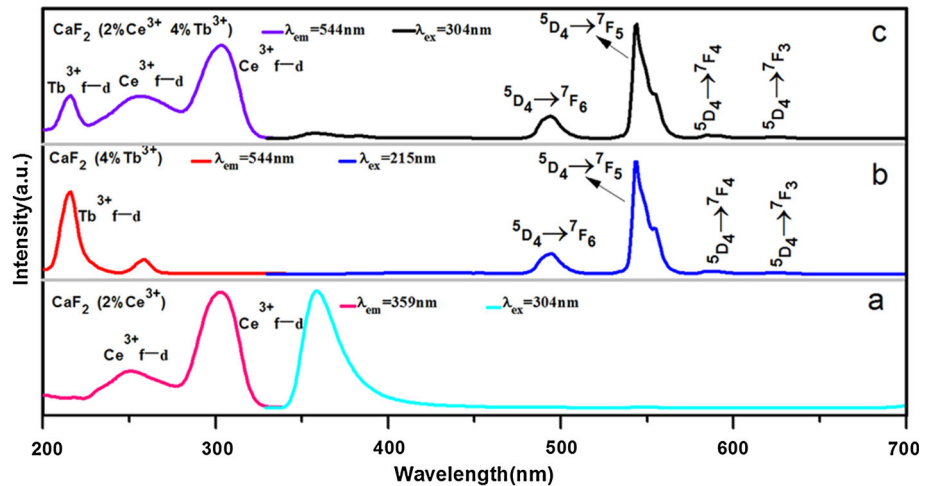
Figure 7 PL spectra of
CaF_2:2%Ce^{3+}/y%Tb^{3+}
phosphors ($\lambda_{ex} = 304$ nm).
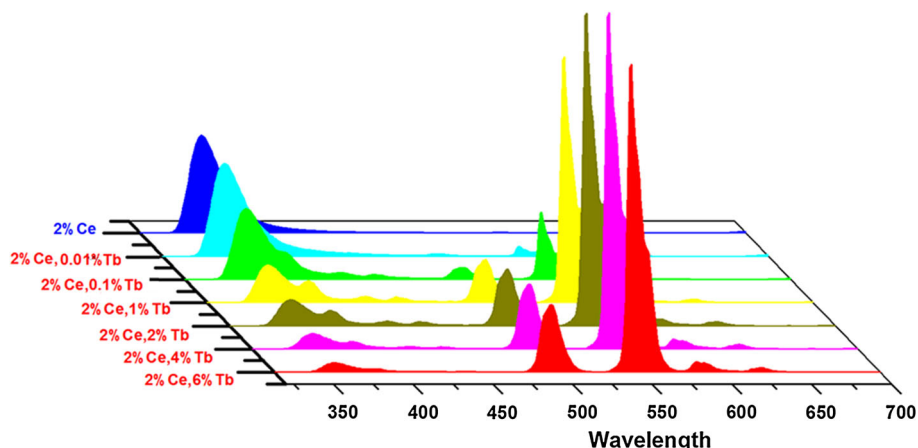
$^5D_4 \rightarrow {}^7F_5$ transition peaks at 544 nm is much higher than that of the other emission lines on account of a magnetic dipole-allowed transition. In order to enhance the absorption intensity in the NUV region for the Tb^{3+} emission, Ce^{3+} ions can be codoped as sensitizers to transfer energy to the Tb^{3+} ions. As given in Fig. 6c, the PLE and PL spectra of the CaF_2:2% Ce^{3+}/4%Tb^{3+} phosphors are investigated. Using 544 nm (Tb^{3+}: $^5D_4 \rightarrow {}^7F_5$ transition) as monitoring wavelength, we can get PLE spectra which contain a weak band at 215 nm, a moderate band at 251 nm and a strong broadband with a maximum at 304 nm. We can easily know that the peak at 215 nm assigns to the $4f^8$–$4f^75d$ transitions of Tb^{3+} ions and the bands at 251 nm and 304 nm belong to 5d–4f transitions of Ce^{3+} ions by contrast with the PLE spectra of CaF_2:2%Ce^{3+} and CaF_2:4%Tb^{3+} samples (Fig. 6a, b). The presence of the excitation bands of Ce^{3+} in the excitation spectrum monitored with Tb^{3+} emission indicates that energy transfer occurs from Ce^{3+} to Tb^{3+} in CaF_2:2%Ce^{3+}/4%Tb^{3+}. Moreover, when excited at 304-nm wavelength from the characteristic absorption peak of Ce^{3+}, the PL spectra of CaF_2:2%Ce^{3+}/4%Tb^{3+} phosphor exhibit not only the weak emission peak in the blue region from the electric-dipole-allowed 4f–5d transitions of Ce^{3+}, but also the strong emission of Tb^{3+} ($^5D_4 \rightarrow {}^7F_{J(J = 6, 5, 4, 3)}$) at 494, 544, 590 and 626 nm), which also provides another evidence for the energy transfer from Ce^{3+} to Tb^{3+} in CaF_2:2%Ce^{3+}/4%Tb^{3+} microspheres.

The PL spectra for CaF_2:2%Ce^{3+}/y%Tb^{3+} ($y = 0.01$–6) samples are shown in Fig. 7. Under excitation at 304 nm, each of the emission spectrum for CaF_2:2%Ce^{3+}/y%Tb^{3+} samples consists of an emission band of Ce^{3+} ions and several emission peaks of Tb^{3+} ions. At the same time, with the increase in the Tb^{3+} concentration ($0.01 \le y \le 4$), the intensity of blue emission at 359 nm decreased monotonously, while the emission intensity of Tb^{3+} increased and reached the maximum at $y = 4$ and then generally decreases due to Tb^{3+} concentration quenching. The shape of corresponding PL spectra remains unchanged when $y = 6$, which suggests that the possible energy-transfer process can exist between Ce^{3+} and Tb^{3+}. The distance between sensitizer Ce^{3+} and activator Tb^{3+} becomes closer with increase of Tb^{3+} ions content, which is beneficial for efficient energy transfer from Ce^{3+} to Tb^{3+} ions. When Tb^{3+} content is beyond the critical concentration ($y = 4$), the emission intensity of Tb^{3+} decreases because of Tb^{3+}–Tb^{3+} internal concentration quenching.

Figure 8a shows the PLE and PL spectrum of CaF_2:4%Tb^{3+}. In the excitation spectrum under monitoring of Tb^{3+} at 544 nm, the PLE spectrum is composed of a strong band at 215 nm and a weak
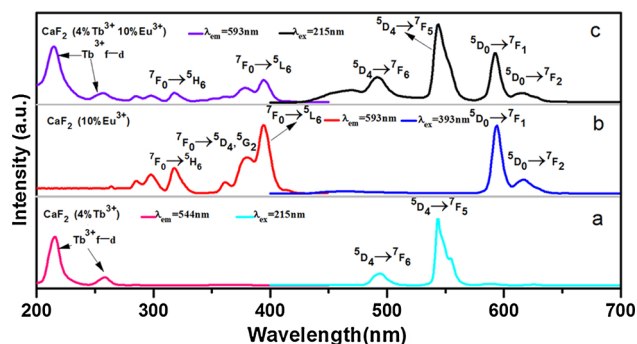

Figure 8 PLE and PL spectra of CaF_2: 4%Tb^{3+} (*a*), 10%Eu^{3+} (*b*) and 4%Tb^{3+}/10%Eu^{3+} (*c*).
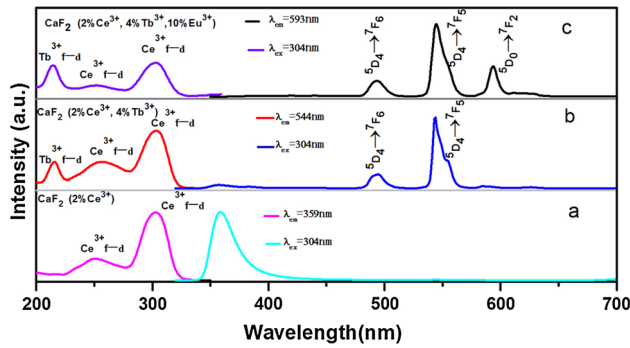
Figure 9 PLE and PL spectra of CaF$_2$: 2%Ce^{3+} (a), 2%Ce^{3+}/4%Tb^{3+} (b), 2%Ce^{3+}/4%Tb^{3+}/10%Eu^{3+} (c).

band at 259 nm attributed to the Tb^{3+} of 4f^8–4f^{7}5d transition. The PL spectrum obtained under the excitation at 215 nm shows characteristic sharp emission lines of Tb^{3+} f → f transitions at 494, 544, 590 and 626 nm which are corresponding to the $^5D_4 \rightarrow {}^7F_{J(J = 6, 5, 4, 3)}$ transitions. The PLE and PL spectra of CaF$_2$:10%Eu^{3+} are shown in Fig. 8b. By monitoring the dominant emission of Eu^{3+} at 593 nm ($^5D_0 \rightarrow {}^7F_1$ transition), the sharp peaks in the range of 200−450 nm are ascribed to the typical intraconfigurational f–f transitions of Eu^{3+} ions. They are the $^7F_0 \rightarrow {}^5H_6$ transition at 318 nm, the $^7F_0 \rightarrow {}^5D_4$ transition at 361 nm, the $^7F_0 \rightarrow {}^5L_6$ transition at 393 nm, respectively. Under 393-nm excitation, the sharp emission peaks at 593 and 617 nm are observed in PL spectrum, which attributed to Eu^{3+} $^5D_0 \rightarrow {}^7F_{J(J = 1, 2)}$ transitions. It is observed that the magnetic dipole $^5D_0 \rightarrow {}^7F_1$ transition at 593 nm is stronger than the electric dipole $^5D_0 \rightarrow {}^7F_2$ transition at 617 nm, which indicate the Eu^{3+} localized in symmetric environment. When doping 10%Eu^{3+} in CaF$_2$:4%Tb^{3+}, the sample shows a red–orange emission under UV excitation. The doped Eu^{3+} affects the matrix's

luminescent properties significantly in the present case. The PLE and PL spectra of the sample are shown in Fig. 8c. In the excitation spectrum of CaF$_2$:4%Tb^{3+}/10%Eu^{3+} under monitoring of Eu^{3+} at 619 nm, the main appearance is similar to that in Fig. 8a except from a few weak transition lines of Eu^{3+} appearing at 318 nm ($^7F_0 \rightarrow {}^5H_6$), 361 nm ($^7F_0 \rightarrow {}^5D_4$) and 393 nm ($^7F_0 \rightarrow {}^5L_6$), respectively. Under 215-nm excitation (4f$^8 \rightarrow$ 4f^7 5d transition of Tb^{3+}), the PL spectrum is consisted of not only the emission of Tb^{3+} ($^5D_4 \rightarrow {}^7F_6$ at 494 nm, $^5D_4 \rightarrow {}^7F_5$ at 544 nm), but also the emission of Eu^{3+} ($^5D_0 \rightarrow {}^7F_1$ at 593 nm, $^5D_0 \rightarrow {}^7F_2$ at 617 nm). The existence of Tb^{3+} f → d transition lines in the excitation spectrum by monitoring the emission of Eu^{3+} ($^5D_0 \rightarrow {}^7F_1$, 593 nm) and the presence of the intense emission lines of Eu^{3+} by exciting into Tb^{3+} (215 nm) both clearly suggest efficient energy transfer from Tb^{3+} to Eu^{3+} in CaF$_2$:4%Tb^{3+}/10%Eu^{3+}.

As discussed by Blasse [35, 40], Tb^{3+} can act as an energy-transfer chain to bridge Ce$^{3+} \rightarrow$Eu^{3+} energy transfer and block the corresponding metal–metal charge transfer (MMCT) process. Figure 9c demonstrates the PLE and PL spectra of CaF$_2$:2%Ce^{3+}/4%Tb^{3+}/10%Eu^{3+}. Under Ce^{3+} excitation band at 304 nm, the synthesized samples exhibit the Eu^{3+} $^5D_0 \rightarrow {}^7F_2$ red emission peaks at 593 nm together with the emission of Tb^{3+} ($^5D_4 \rightarrow {}^7F_6$ at 494 nm, $^5D_4 \rightarrow {}^7F_5$ at 544 nm), while the Ce^{3+} emission suffers obvious quenching. As shown in Fig. 9c, the CaF$_2$:2%Ce^{3+}/4%Tb^{3+}/10%Eu^{3+} possesses an excitation spectrum which is similar to that of CaF$_2$:2%Ce^{3+}/4%Tb^{3+}. By monitoring the dominant emission at 593 nm (Eu^{3+}: $^5D_0 \rightarrow {}^7F_2$), the PLE spectrum consists of Ce^{3+} f → d and Tb^{3+} f → d excitation bands. These results give a direct evidence of Eu^{3+} sensitized by Ce$^{3+} \rightarrow$Tb$^{3+} \rightarrow$ Eu^{3+} energy transfer.

Figure 10 The calculated energy-transfer efficiencies for Ce^{3+} → Tb^{3+} in CaF$_2$:2%Ce^{3+}/y%Tb^{3+} (a) and Tb^{3+}→ Eu^{3+} in CaF$_2$:2%Ce^{3+}/4%Tb^{3+}/z%Eu^{3+} (b).
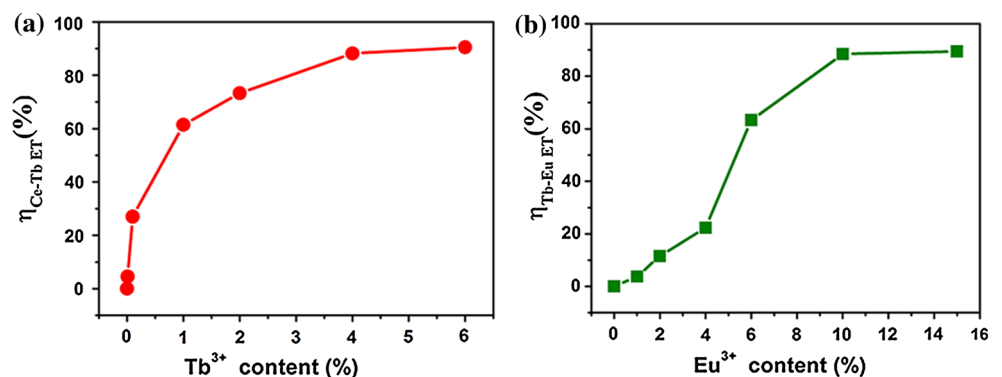
To better understand the energy-transfer process, the energy-transfer efficiency (η_{ET}) from sensitizer ions to activator ions can be calculated by the following formula [41]:

$$\eta_{ET} = 1 - I/I_0 \qquad (4)$$

where η_{ET} is the energy-transfer efficiency and I and I_0 are the emission intensities of the sensitizer in the presence and the absence of an activator, respectively. As shown in Fig. 10, by monitored at 304 nm of CaF$_2$: 2% Ce^{3+}/y%Tb^{3+} phosphor and CaF$_2$: 2% Ce^{3+}/4%Tb^{3+}/z% Eu^{3+} phosphor, we can obtain the peak value of corresponding emission band at 359 nm (Ce^{3+} emission) and 544 nm (Tb^{3+} emission) which can be regarded as "I" for calculating Ce^{3+}→Tb^{3+} energy-transfer efficiency and Tb^{3+}→Eu^{3+} energy-transfer efficiency, respectively. As shown in Fig. 10a, the energy-transfer efficiencies from Ce^{3+} to Tb^{3+} in CaF$_2$: 2% Ce^{3+}/y% Tb^{3+} can be found to increase gradually with concentration of Tb^{3+} from 0 to 6 and the corresponding value of η_{ET} is calculated to be 0, 4.6, 27, 61.4, 73.3, 84.2, 90.5%, which provide additional evidence of the energy transfer between Ce^{3+} and Tb^{3+} [3]. Figure 10b shows the η_{ET} for further Tb^{3+}→Eu^{3+} energy transfer which is a relative function of the Eu^{3+} concentration. It was found that the η_{ET} increases from 0 to 89.5% with the increase of Eu^{3+} content in CaF$_2$:2% Ce^{3+}/4%Tb^{3+}/z% Eu^{3+} phosphors. When z = 15, the maximum value of η_{ET} is calculated to be 89.5%. The obtained results prove that the energy-transfer process from Tb^{3+} to Eu^{3+} is very efficient. From above, we can draw a conclusion that Tb^{3+}-doped content is an critical factor for blocking the MMCT process between Ce^{3+} and Eu^{3+} and realizing an efficient Tb^{3+}→Eu^{3+} energy transfer [42].

In order to further study the tunable PL properties and energy-transfer process, the decay time of CaF$_2$:2%Ce^{3+}/y%Tb^{3+}/z%Eu^{3+} phosphors was also investigated to obtain information on the Ce^{3+}→Tb^{3+} and Tb^{3+}→Eu^{3+} energy transfer. The decay curves of Ce^{3+} in CaF$_2$:2% Ce^{3+}, y%Tb^{3+}(y = 0 and 4), Tb^{3+} in CaF$_2$:4%Tb^{3+}, z%Eu^{3+}(z = 0 and 10) and Tb^{3+} in CaF$_2$:2%Ce^{3+}, 4%Tb^{3+}, z%Eu^{3+} (z = 0 and 10) phosphors are demonstrated in Fig. 11. As is known to all, when the radiative energy-transfer processes play a major role in specific materials, the acceptor makes no difference on the decay time of a donor. Nevertheless, when the nonradiative energy-transfer
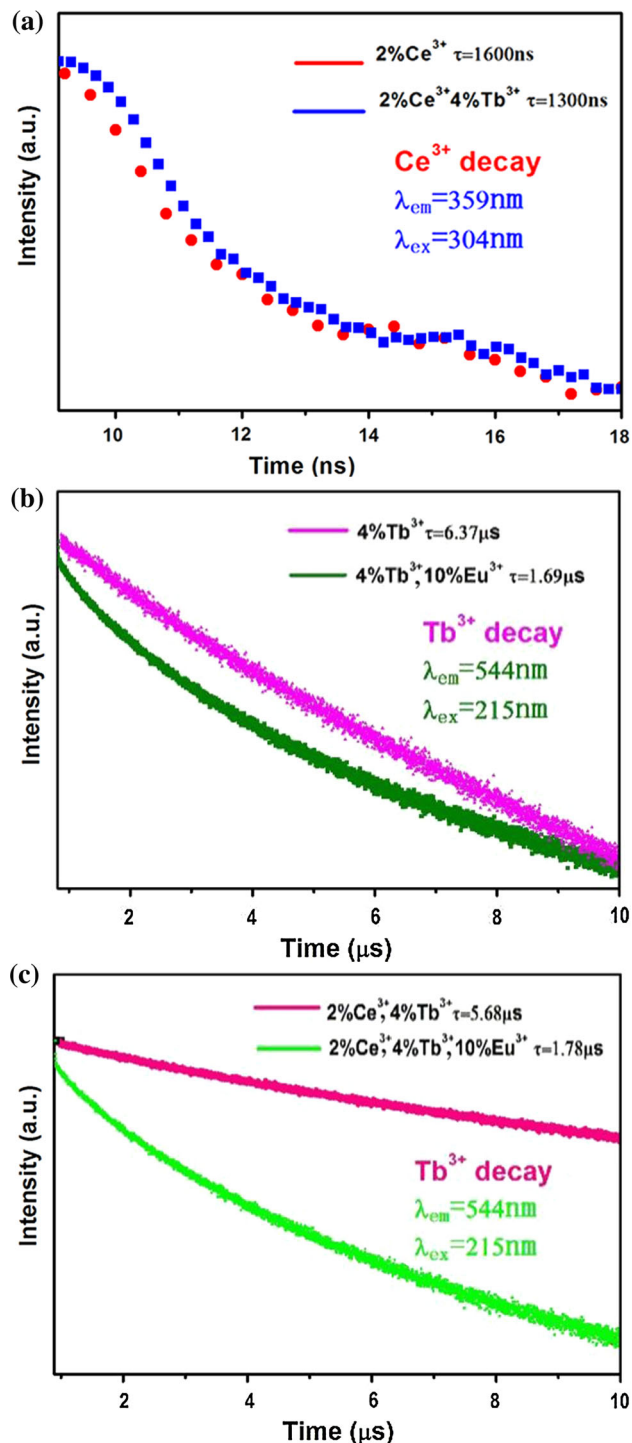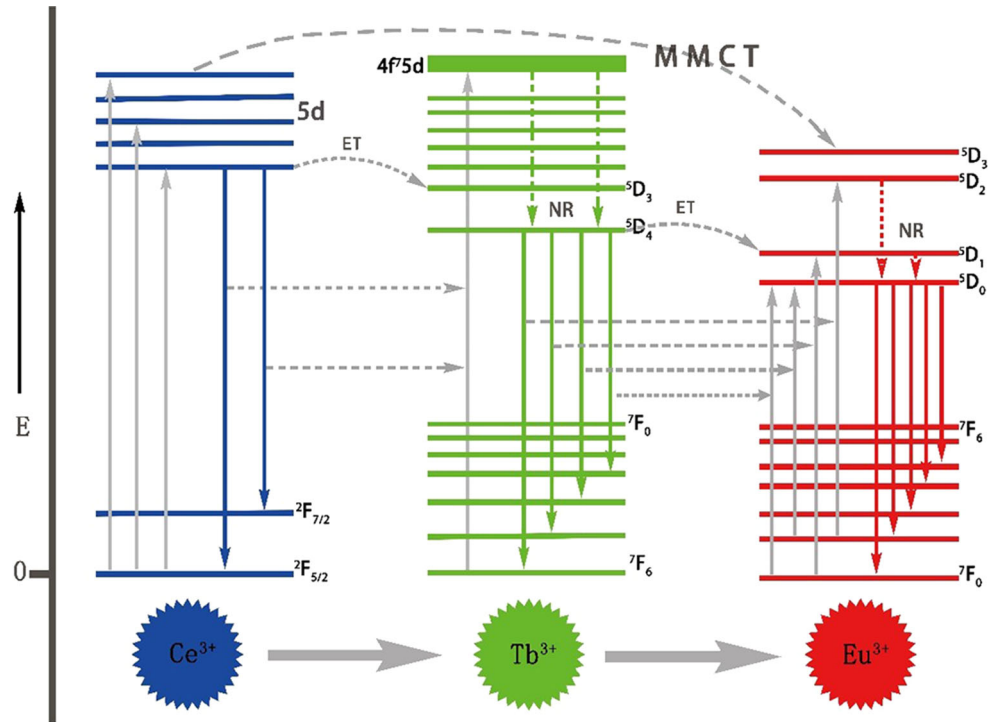

Figure 11 The decay curves of Ce^{3+} in CaF$_2$:2% Ce^{3+}/4%Tb^{3+} (a), Tb^{3+} in CaF$_2$:4%Tb^{3+}/10%Eu^{3+} (b) and Tb^{3+} emission in CaF$_2$: 2%Ce^{3+}/4%Tb^{3+}/10%Eu^{3+} (c) phosphors.

processes have a principal position, the concentration of acceptor has a great impact on the decay time of a donor. The decay time of the donor decreases

Figure 12 Energy level model for the ET processes of $Ce^{3+} \rightarrow Tb^{3+} \rightarrow Eu^{3+}$ in CaF_2 host.

gradually with the increasing concentration of acceptor [40, 41].

The decay curves and lifetime of Ce^{3+} in CaF_2:2% Ce^{3+}, $y\%Tb^{3+}$ ($y = 0, 4$) are exhibited in Fig. 11a. It can be seen that the decay curves are well fitted with the following double exponential equation:

$$I = A_1 \exp(-t/\tau_1) + A_2 \exp(-t/\tau_2) \qquad (5)$$

Here I is the luminescence intensity; A_1 and A_2 are two constants which are related with the initial intensity; t is time; τ_1 and τ_2 are the lifetimes for the exponential components. The average lifetime ($\tau*$) can be calculated using the following equation:

$$\tau* = \left(A_1\tau_1^2 + A_2\tau_2^2\right) / \left(A_1\tau_1 + A_2\tau_2\right) \qquad (6)$$

When only Ce^{3+} ions doped in CaF_2 phosphor, the lifetime of the Ce^{3+} is 1600 ns. However, the lifetime of Ce^{3+} decreases (1300 ns) with the introduction of Tb^{3+} which proves the energy transfer from Ce^{3+} to Tb^{3+} through nonradiative process.

The decay curves of Tb^{3+} in the CaF_2:4% Tb^{3+}, $z\%Eu^{3+}$ (Fig. 11b) and CaF_2:2% Ce^{3+},4% Tb^{3+}, $z\%Eu^{3+}$(Fig. 11c) well fit a typical single exponential function as:

$$I_t = I_0 \exp(-t/s) \qquad (7)$$

The lifetime of Tb^{3+} in CaF_2: 4% Tb^{3+} was compared with that in CaF_2:4% Tb^{3+}, 10% Eu^{3+}, as shown in

Fig. 11b. The lifetime of Tb^{3+} was shortened from 6.37 μs to 1.69 μs. This result indicates that the shortened decay time of Tb^{3+} emission with increasing Eu^{3+} ions is attributed to the energy transfer from Tb^{3+} to Eu^{3+} in CaF_2:4% Tb^{3+}, $z\%Eu^{3+}$ phosphor. The energy transfer of $Ce^{3+} \rightarrow Tb^{3+} \rightarrow Eu^{3+}$ through nonradiative process can be further proved from the fact that the lifetime of Tb^{3+} (5.68 μs) declines with the introduction of Eu^{3+} (1.78 μs). With higher Eu^{3+} concentration, it is hard to get the lifetime of Ce^{3+} because of too weak signal of Ce^{3+} emission.

The proposed energy level model for the ET processes of $Ce^{3+} \rightarrow Tb^{3+} \rightarrow Eu^{3+}$ in the CaF_2 host is demonstrated in Fig. 12. Firstly, Ce^{3+} ions can be effectively excited from the ground state ($^2F_{5/2}$) to the excited states (5d energy levels) by UV irradiation. Later on, Ce^{3+} ions either get back to the lowest vibrational level of the excited state giving out the excess energy to their surroundings or return to the ground states ($^2F_{7/2}$ and $^2F_{5/2}$) spontaneously by a radiative process. The phosphor emits blue light or transfer their excitation energy to $^5D_3$ level of Tb^{3+} ions, followed by nonradiative relaxation to $^5D_4$ level ($^5D_3 + {}^7F_6 = {}^5D_4 + {}^7F_0$) due to the same energy difference between $^5D_3 \rightarrow {}^5D_4$ and $^7F_0 \rightarrow {}^7F_6$ in Tb^{3+} ions [41]. Then, as a result of the electrons moving

from the $^5D_4$ excited state to the $^7F_{J(J\,=\,3,\,4,\,5,\,6)}$ ground state, green light is obtained. Meanwhile, the excitation energy on $^5D_4$ level of Tb^{3+} transfers to higher excited energy level of Eu^{3+} ($^4f_6$) through cross-relaxation and then relaxes to the $^5D_0$ level of Eu^{3+} and gives out red emission due to $^5D_0 \rightarrow {}^7F_{J(J\,=\,0,\,1,\,2)}$ transitions [42].

Conclusion

The CaF_2:Ce^{3+}, Tb^{3+}, Eu^{3+} phosphors with homogeneous, monodispersed and well-defined morphology were synthesized by a simple hydrothermal method. The pH, organic additive and reaction time have significant influences on the phase and shape of the obtained products. The energy transfer of $Ce^{3+} \rightarrow Tb^{3+} \rightarrow Eu^{3+}$ through nonradiative process has been investigated in CaF_2, which exhibits strong and broad excitation band in NUV region. The Ce^{3+} ions act as a good sensitizer and transfer most part of their energy to the activator ions. The efficient color-tunable emission can be generated from blue to green to red with increase of Tb^{3+} and Eu^{3+} in the CaF_2:Ce^{3+} phosphors. The results also indicate that CaF_2:Ce^{3+}, Tb^{3+}, Eu^{3+} phosphors will have promising applications in field of near-UV and violet LEDs.

Acknowledgements

Electronic supplementary material: The online version of this article (doi:10.1007/s10853-017-0822-2) contains supplementary material, which is available to authorized users.

References

[1] Quan ZW, Xu HW, Wang CY, Wen XD, Wang YX, Zhu JL, Li RP, Sheehan CJ, Wang ZW, Smilgies DM, Luo ZP, Fang JY (2014) Solvent-mediated self-assembly of nanocube superlattices. J Am Chem Soc 136:1352–1359

[2] Dong H, Li XJ, Peng Q, Wang X, Chen JP, Li YD (2005) Monodisperse magnetic single-crystal ferrite microspheres. Angew Chem Int Ed 44:2782–2785

[3] Li G, Hou Z, Peng C, Wang W, Cheng Z, Li C, Lian H, Lin J (2010) Electrospinning derived one-dimensional LaOCl: Ln^{3+} (Ln = Eu/Sm, Tb, Tm) nanofibers, nanotubes and microbelts with multicolor-tunable emission. Adv Funct Mater 20:3446–3456

[4] Huang CH, Chan TS, Liu WR, Wang D, Chiu YC, Ye H, Yeh YT, Chen TM (2012) Crystal structure of blue–white–yellow color-tunable Ca4Si2O7F2:Eu^{2+}, Mn^{2+} phosphor and investigation of color tunability through energy transfer for single-phase white-light near-ultraviolet LEDs. J Mater Chem 22:20210–20216

[5] Zhang Y, Geng DL, Kang XJ, Shang MM, Wu Y, Li XJ, Lian HZ, Cheng ZY, Lin J (2013) Rapid, large-scale, morphology-controllable synthesis of YOF:Ln^{3+}(Ln = Tb, Eu, Tm, Dy, Ho, Sm) nano-/microstructures with multicolor tunable emission properties. Inorg Chem 52:12986–12994

[6] Wang LS, Zhou YH, Quan ZW, Lin J (2005) Formation mechanisms and morphology dependent luminescence properties of Y_2O_3:Eu phosphors prepared by spray pyrolysis process. Mater Lett 59:1130–1133

[7] Li JG, Li X, Sun X, Ishigaki TJ (2008) Monodispersed colloidal spheres for uniform Y_2O_3:Eu^{3+} red-phosphor particles and greatly enhanced luminescence by simultaneous Gd^{3+} doping. Phys Chem C 112:11707–11716

[8] Wang H, Lin CK, Liu XM, Lin J (2005) Monodisperse spherical core-shell-structured phosphors obtained by functionalization of silica spheres with Y_2O_3:Eu^{3+} layers for field emission displays. Appl Phys Lett 87:181907

[9] Song KC, Kang Y (2000) Preparation of high surface area tin oxide powders by a homogeneous precipitation method. Mater Lett 42:283–289

[10] Feng W, Sun LD, Zhang YW, Yan CH (2010) Synthesis and assembly of rare earth nanostructures directed by the principle of coordination chemistry in solution-based process. Coord Chem Rev 254:1038–1053

[11] Zhou L, Hu SS, Zhou XJ, Tang JF, Yang J (2016) One-step surfactant-free synthesis of Eu^{3+} activated NaTb(MoO4)$_2$ microcrystals with controllable shape and their multicolor luminous properties. CrystEngComm 8:7590–7600

[12] Mao YB, Zhang F, Wong SS (2006) Ambient template-directed synthesis of single-crystalline alkaline-earth metal fluoride nanowires. Adv Mater 18:1895–1899

[13] Wang WS, Zhen L, Xu CY, Chen JZ, Shao WZ (2009) Aqueous solution synthesis of CaF_2 hollow microspheres via the Ostwald ripening process at room temperature. ACS Appl Mater Interfac 1:780–788

[14] Feldmann C, Roming M, Trampert K (2006) Polyol-mediated synthesis of nanoscale CaF$_2$ and CaF$_2$:Ce, Tb. Small 2:1248–1250

[15] Liu YS, Tu DT, Zhu HM, Ma E, Chen XY (2013) Lanthanide-doped luminescent nano-bioprobes: from fundamentals to biodetection. Nanoscale 5:1369–1384

[16] Gao P, Xie Y, Li Z (2006) Controlling the size of BaF$_2$ nanocubes from 1000 to 10 nm. Eur J Inorg Chem 2006:3261–3265

[17] Quan ZW, Yang PP, Li CX, Yang J, Yang DM, Jin Y, Lian HZ, Li HY, Lin J (2009) Shape and phase-controlled synthesis of KMgF$_3$ colloidal nanocrystals via microwave irradiation. J Phys Chem C 113:4018–4025

[18] Sokolov NS, Suturin SM (2000) MBE-growth peculiarities of fluoride (CdF$_2$–CaF$_2$) thin film structures. Thin Solid Films 367:112–119

[19] Pilvi T, Arstila K, Leskel M, Ritala M (2007) Novel ALD process for depositing CaF$_2$ thin films. Chem Mater 19:3387–3392

[20] Sun XM, Li YD (2003) Size-controllable luminescent single crystal CaF2 nanocubes. Chem Commun 17:1768–1769

[21] Quan ZW, Yang DM, Yang PP, Zhang XM, Lian HZ, Liu XM, Lin J (2008) Uniform colloidal alkaline earth metal fluoride nanocrystals: nonhydrolytic synthesis and luminescence properties. Inorg Chem 47:9509–9517

[22] Blednov AV, Gorbenko OY, Samoilenkov SV, Amelichev VA, Lebedev VA, Napolskii KS, Kaul AR (2010) Epitaxial calcium and strontium fluoride films on highly mismatched oxide and metal substrates by MOCVD: texture and morphology. Chem Mater 22:175–185

[23] Zhang XM, Quan ZW, Yang J, Yang PP, Lian HZ, Lin J (2008) Solvothermal synthesis of well-dispersed MF$_2$ (M = Ca, Sr, Ba) nanocrystals and their optical properties. Nanotechnology 19:075603

[24] Pandurangappa C, Lakshminarasappa BN, Nagabhushana BM (2010) Synthesis and characterization of CaF2 nanocrystals. J Alloys Compd 489:592–595

[25] Cao CY, Qin WP, Zhang JS, Wang Y, Wang GF, Wei GD, Zhu PF, Wang LL, Jin LZ (2008) Up-conversion white light of Tm^{3+}/Er^{3+}/Yb^{3+} tri-doped CaF$_2$ phosphors. Opt Commun 281:1716–1719

[26] Setlur AA, Heward WJ, Gao Y, Srivastava AM (2006) Crystal chemistry and luminescence of Ce^{3+}-doped Lu$_2$CaMg$_2$(Si, Ge)3O$_{12}$ and its use in LED based lighting. Chem Mater 18:3314–3322

[27] Ye S, Xiao F, Pan Y, Ma Y, Zhang Q (2010) Phosphors in phosphorconverted white light-emitting diodes: recent advances in materials, techniques and properties. Mater Sci Eng R 71:1–34

[28] Xia ZG, Liu RS (2012) Tunable blue–green color emission and energy transfer of Ca$_2$Al$_3$O$_6$F:Ce^{3+}, Tb^{3+} phosphors for near-UV white LEDs. J Phys Chem C 116:15604–15609

[29] Blasse G (1991) Optical electron transfer between metal ions and its consequences. Struct Bonding 76:153–187

[30] Setlur AA (2012) Sensitizing Eu^{3+} with Ce^{3+} and Tb^{3+} to make narrow-line red phosphors for light emitting diodes. Electrochem Solid State Lett 15:J25–J27

[31] Zhang CM, Li CX, Peng C, Chai RT, Huang SS, Yang DM, Cheng ZY, Lin J (2010) Facile and controllable synthesis of monodisperse CaF$_2$ and CaF$_2$:Ce^{3+}/Tb^{3+} hollow spheres as efficient luminescent materials and smart drug carriers. Chem Eur J 16:5672–5680

[32] Zheng W, Zhou SY, Chen Z, Hu P, Liu YS, Tu DT, Zhu HM, Li RF, Huang MD, Chen XY (2013) Sub-10 nm lanthanide-doped CaF$_2$ nanoprobes for time-resolved luminescent biodetection. Angew Chem 125:6803–6808

[33] Ritter BJ, Thoralf KK, Rurackand EK (2014) Nanoscale CaF$_2$ doped with Eu^{3+} and Tb^{3+} through fluorolytic sol–gel-synthesis. J Mater Chem C 2:8607

[34] Chen LM, Hong ZR, Li G, Yang Y (2009) Recent progress in polymer solar cells: manipulation of polymer: fullerene morphology and the formation of efficient inverted polymer solar cells. Adv Mater 21:1434–1449

[35] Zhang XG, Zhou LY, Pang Q, Shi JX, Gong MG (2014) Tunable luminescence and Ce^{3+} → Tb^{3+} → Eu^{3+} energy transfer of broadband-excited and narrow line red emitting Y$_2$SiO$_5$:Ce^{3+}, Tb^{3+}, Eu^{3+} Phosphor. J Phys Chem C 118:7591–7598

[36] Li CX, Quan ZW, Yang PP, Huang SS, Lian HZ, Lin J (2008) Shape-controllable synthesis and upconversion properties of lutetium fluoride (doped with Yb^{3+}/Er^{3+}) microcrystals by hydrothermal process. J Phys Chem C 112:13395–13404

[37] Xu L, Yang XY, Zhai Z, Chao X, Zhang ZH, Hou WH (2011) EDTA-mediated hydrothermal synthesis of NaEu(MoO$_4$)$_2$ microrugbies with tunable size and enhanced luminescence properties. CrystEngComm 13:4921–4929

[38] Luo Y, Yang RH, Zhang XL, Hu B, Hu SS, Zhou L, Yang J (2015) Shape-controllable hydrothermal synthesis of NaTbF$_4$:Eu^{3+} microcrystals with energy transfer from Tb to Eu and multicolor luminescence properties. CrystEngComm 17:7762–7771

[39] Zhao B, Yuan L, Hu SS, Zhang XM, Zhou XJ, Tang JF, Yang J (2016) One-step hydrothermal synthesis of Sc$_2$Mo$_3$O$_{12}$:Ln^{3+} (Ln = Eu, Tb, Dy, Tb/Eu, Dy/Eu) nanosheets and their multicolor tunable luminescence. New J Chem 40:9211–9222

[40] Zhang XG, Gong ML (2015) Photoluminescence and energy transfer of Ce^{3+}, Tb^{3+}, and Eu^{3+} doped KBaY(BO$_3$)$_2$ as

near ultraviolet-excited color-tunable phosphors. Ind Eng Chem Res 54:7632–7639

[41] Wen DW, Shi JX (2013) A novel narrow-line red emitting Na2Y2B2O7:Ce^{3+}, Tb^{3+}, Eu^{3+} phosphor with high efficiency activated by terbium chain for near-UV white LEDs. Dalton Trans 42:16621–16629

[42] Zhou J, Xia Z (2015) Luminescence color tuning of Ce^{3+}, Tb^{3+} and Eu^{3+} codoped and tri-doped BaY$_2$Si$_3$O$_{10}$ phosphors via energy transfer. J Phys Chem C 3:7552–7560